MOX-Report No. 13/2020

A data-driven surrogate model for fluid-structure interaction in carotid arteries with plaque

Pozzi S.; Domanin M.; Forzenigo L.; Votta E.; Zunino P.;

Redaelli A.; Vergara C.

MOX, Dipartimento di Matematica
Politecnico di Milano, Via Bonardi 9 - 20133 Milano (Italy)

mox-dmat@polimi.it http://mox.polimi.it

A data-driven surrogate model for fluid-structure interaction in carotid arteries with plaque

Silvia Pozzi [1], Maurizio Domanin [2,3], Laura Forzenigo [4], Emiliano Votta [5], Paolo Zunino [5], Alberto Redaelli [4], Christian Vergara [6]

February 20, 2020

[1] MOX – Modellistica e Calcolo Scientifico
Dipartimento di Matematica, Politecnico di Milano
silvia.pozzi@polimi.it, paolo.zunino@polimi.it

[2] Department of Clinical Sciences and Community Health
Università di Milano
maurizio.domanin@unimi.it

[3] Unità Operativa di Chirurgia Vascolare
Fondazione I.R.C.C.S. Cà Granda, Ospedale Maggiore Policlinico

[4] Unità Operativa di Radiologia
Fondazione I.R.C.C.S. Cà Granda, Ospedale Maggiore Policlinico
lvforzenigo@gmail.com

[5] Department of Electronics, Information and Bioengineering
Politecnico di Milano
emiliano.votta@polimi.it, alberto.redaelli@polimi.it

[6] LaBS, Dipartimento di Chimica, Materiali e Ingegneria Chimica "Giulio Natta"
Politecnico di Milano
christian.vergara@polimi.it

Keywords: Atheromasic plaque, carotid arteries, fluid-structure interaction, CINE MRI images, Robin boundary condition.

Abstract

In this work, we propose a surrogate model for the Fluid-Structure Interaction (FSI) problem for the study of blood dynamics in carotid arteries in presence of plaque. This model is based on the integration with subject-specific data and clinical imaging. In more detail, we propose to model the atherosclerotic plaque as part of the tissues surrounding the vessel wall through the application of an elastic support boundary condition on the external surface of the structure model. In order to characterize the plaque and other surrounding tissues, such as the close-by jugular vein, the elastic parameter of the boundary condition was spatially differentiated. The

values of these parameters were estimated by minimizing the discrepancies between computed vessel wall displacements and reference values obtained from CINE Magnetic Resonance Imaging (MRI) data. As a first application of the method, we considered three subjects with a degree of stenosis greater than 70%. We found that accounting for both plaque and jugular vein in the estimation of the elastic parameters increases the accuracy. In particular, in all patients, mismatches between computed and *in vivo* measured wall displacements were 1-2 orders of magnitude lower than the spatial resolution of the original MRI data. These results confirmed the validity of the proposed surrogate model.

1 Introduction

Carotid arteries represent a preferential site for the development of atherosclerotic plaques. Currently, plaque stenosis severity is the main criterion used to inform clinical decisions regarding treatment (Naylor et al. 2017), such as carotid artery stenting and carotid endarterectomy.

Imaging acquisitions such as Echo-Color Doppler (ECD), Magnetic Resonance Imaging (MRI) and Computed Tomography (CT) are widely regarded as reliable tools to evaluate the severity of the stenosis. Many studies, however, suggest that purely morphological evaluations could have limitations for clinical diagnosis, treatment selection, and surgery planning (Makris et al. 2010; Tang et al. 2014). In fact, plaque development, progression and risk of rupture have been linked not only to arterial geometry, but also to hemodynamic and mechanical features. For example, low and oscillating Wall Shear Stress (WSS) has been shown to correlate positively with intimal thickening (Hyun et al. 2000; Meyerson et al. 2001; Heise et al. 2003; Morbiducci et al. 2010) and atherosclerosis initiation (Zarins et al. 1983; Ku et al. 1985; Nixon et al. 2009). In presence of atherosclerotic plaque, peak systolic velocity (PSV) higher than $200\,cm/s$ and high values of WSS are considered as fluid-dynamics indicators that enhance plaque vulnerability, increasing the risk of plaque rupture (Slager et al. 2005; Mofidi et al. 2005; Groen et al. 2007).

To evaluate fluid-dynamic quantities, Phase Contrast (PC) MRI is considered a very promising and reliable imaging tool. This technique has proven suitable for flow velocity measurements in healthy subjects (Markl et al. 2010; Ponzini et al. 2010). However, due to the high spatial and temporal resolutions needed for a thorough analysis of stenotic carotids, PC MRI could lead to a slight underestimation of the flow patterns in such districts (Baltes et al. 2008).

For the reasons mentioned above, *image-based computational modeling* represents an effective tool to characterize fluid-dynamics with high spatial and temporal resolutions, required especially in pathological cases. In particular, Computational Fluid Dynamics (CFD) has been used for the study of carotid blood dynamics since the early '90s (see e.g. Perktold and Resch 1990). In the last three decades a lot of progress has been made and nowadays several indica-

tions can be provided to clinicians in view of their decisions (see e.g. Hyun et al. 2003; Thomas et al. 2005; Kamenskiy et al. 2013; Harrison et al. 2014; Domanin et al. 2017b,a).

Many studies have been proposed to assess stenotic carotids by means of CFD (Rossmann et al. 2002; Lee et al. 2008; Groen et al. 2010; Sui et al. 2014; Guerciotti et al. 2015). More precisely, such works investigate the contribution of blood dynamic indices such as WSS to the pathophysiological processes linked with atherosclerosis and to plaque rupture risk.

In order to obtain more accurate results, several works introduced Fluid-Structure Interaction (FSI) models for stenotic carotids (see e.g Tang et al. 2004; Gao et al. 2009; Kock et al. 2008; Wang et al. 2017). Regarding the plaque, different approaches have been considered in order to account for the changes in geometry and mechanical properties determined by its morphology and composition. In Lee et al. 2012, the changes in geometry are modeled through the inclusion of a stenosis in the fluid lumen. The presence of the plaque is however ignored in the structure model, where no atheromasic region or specific mechanical characterization is considered. Instead, in Tao et al. 2015, the geometric contribution of the plaque is considered also in the structure by means of the reconstruction of a thickened atheromasic region. However, no specific mechanical characterization is introduced, as the atheromasic tissue is embedded as part of the healthy tissue. Finally, we mention more complete studies in which the plaque is included in the model by means of a multi-component structure (Tang et al. 2004; Leach et al. 2009; Wang et al. 2017), made up of elements such as a lipid-rich necrotic core and calcifications. In these works, the detailed modeling of the plaque allows for a better understanding of both blood dynamics and mechanical behaviour. Hovever, the different elements are delineated from multi-contrast MRI images, a technique not widely available in the clinical practice. This aspect, and the irregularities in plaque morphology, make the reconstruction of the plaque a challenging task. To overcome this issue, a recent strategy to outline the plaque region is based on assuming the diameter of the originally healthy internal wall in correspondence of the stenosis, and considering the area between healthy and stenotic wall as the plaque region (Xu et al. 2020).

In an effort to reduce the complexity related to the modeling of the atherosclerotic plaque, in this work we propose a surrogate model able to accurately describe the influence of the plaque on blood dynamics. In more detail, we propose an effective FSI model based on substituting the plaque region with a set of independent springs applied at the external surface of the stenotic carotid wall (see Fig. 1), thus surrogating the presence of the atheromasic tissue. This model relies on the prescription of a Robin boundary condition for the structure problem applied at the external surface, as done in Moireau et al. 2011 to account for the surrounding tissues, with however a specific elastic parameter to characterize the plaque.

The elastic spring parameter value was estimated by comparing the *in vivo*

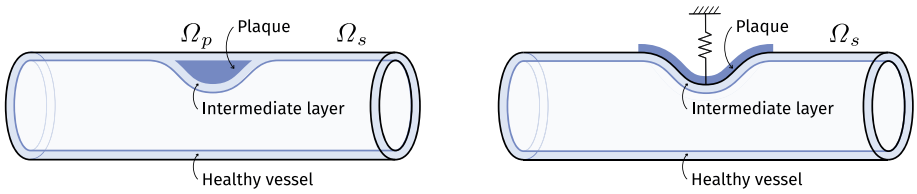

Figure 1: Complete (left) and surrogate (right) plaque models.

lumen-wall boundary displacements obtained from CINE MRI acquisitions with the computed ones. A similar approach was also used to account for the deformable constraint exerted by the adjacent jugular vein. We believe that this model could be of particular interest when one is focused only on fluid-dynamics results, significantly reducing the complexity of the model.

We labeled our approach as data-driven because we are integrating computational modeling and clinical imaging to adapt our new surrogate model to patient-specific cases. In particular, we reconstructed patient-specific geometries, we estimated the spring parameters and we applied inlet boundary conditions by processing three-dimensional MRI images and ECD measurements, respectively.

The outline of the paper is as follows. In Section 2 we introduce the mathematical model for blood dynamics in carotids in presence of plaque and we briefly detail the numerical methods. In Section 3, we describe the image data processing, in particular the analysis of CINE MRI for the estimation of the parameters. Finally, in Section 4 we present numerical results related to three cases with patient-specific ECD and MRI data, which highlight the reliability of the proposed method when used in a real setting of clinical data.

2 Mathematical and numerical model

In medium and large arteries like carotids, blood can be modeled as a homogeneous, incompressible, Newtonian fluid, whereas the vessel wall as an hyperelastic material. When modeling the plaque, a standard approach consists in using the same constitutive law for healthy and atheromasic tissue, and in differentiating the corresponding parameters (Tang et al. 2004, 2013; Yuan et al. 2015).

Here, we chose to model the plaque as a part of the surrounding tissues (see Fig. 1), whose support was modeled as a Robin boundary condition at the external surface of the arterial wall, as proposed in Moireau et al. 2011. This allowed us to avoid the three-dimensional reconstruction of the plaque itself, while still taking into account the influence of plaque morphology through a stenosis in the fluid lumen. Both for calcific and lipidic plaques, the thin intermediate layer of tissue present between the lumen and the core of the plaque (for example given by the fibrous cap) can be assimilated to the healthy tissue

from the mechanics point of view (Brinjikji et al. 2016). Accordingly, many studies account for this by using the same mechanical properties in this layer and in the healthy vessel (Tang et al. 2004; Wang et al. 2017).

Starting from this, we propose to differentiate the elastic parameter in the Robin boundary condition for the structure problem, describing the support of surrounding tissues, in correspondence of the plaque. In such a way, we modeled the core of the plaque as a boundary condition and we characterized the intermediate layer as the healthy vessel (see Fig. 1). We also differentiated the support provided by the close-by jugular vein with respect to the other tissues. We estimated the elastic parameters corresponding to the surrounding tissues (α_s), the jugular vein (α_j) and the plaque (α_p), by prescribing patient-specific inlet flow rates obtained from ECD and by minimizing the discrepancy of the computed wall displacements with measurements obtained from CINE MRI data of the patient.

2.1 Surrogate mathematical model of the plaque

In accordance with the previous discussion, we consider the time-varying domains $\Omega_f^t \subset \mathbb{R}^3$ and $\Omega_s^t \subset \mathbb{R}^3$, representing the lumen of the vessel and the vessel wall, respectively (see Fig. 2). Let Σ^t be the interface between the fluid and the structure domains, and $\Sigma_{ext,s}^t$, $\Sigma_{ext,j}^t$ and $\Sigma_{ext,p}^t$ be the external surface regions in correspondence of the healthy vessel wall, the jugular vein contact area and the plaque, respectively. We define $\boldsymbol{n}$ as the normal unit vector pointing outward with respect to the structure domain. Since we work in a moving domain, the fluid problem was written in an *Arbitrary Lagrangian-Eulerian* (ALE) framework (Hirt et al. 1974; Donéa et al. 1982), whereas solid quantities in the Lagrangian frame (denoted by $\widehat{\ }$).

The coupled problem at each time $t > 0$ reads as follows: find blood velocity $\boldsymbol{u} = \boldsymbol{u}(t, \boldsymbol{x})$, blood pressure $p = p(t, \boldsymbol{x})$, structure displacement $\boldsymbol{d} = \boldsymbol{d}(t, \boldsymbol{x})$ and fluid domain displacement $\boldsymbol{d}_f = \boldsymbol{d}_f(t, \boldsymbol{x})$, such that:

$$\rho_f \left(\frac{\partial \boldsymbol{u}}{\partial t} + ((\boldsymbol{u} - \boldsymbol{u}_f) \cdot \nabla)\, \boldsymbol{u} \right) - \nabla \cdot \boldsymbol{T}_f(\boldsymbol{u}, p) = \boldsymbol{0} \qquad \text{in } \Omega_f^t, \tag{1a}$$

$$\nabla \cdot \boldsymbol{u} = 0 \qquad \text{in } \Omega_f^t, \tag{1b}$$

$$\boldsymbol{u} = \frac{\partial \boldsymbol{d}}{\partial t} \qquad \text{on } \Sigma^t, \tag{1c}$$

$$\boldsymbol{T}_s(\boldsymbol{d})\boldsymbol{n} = \boldsymbol{T}_f(\boldsymbol{u}, p)\boldsymbol{n} \qquad \text{on } \Sigma^t, \tag{1d}$$

$$\rho_s \frac{\partial^2 \widehat{\boldsymbol{d}}}{\partial t^2} - \nabla \cdot \widehat{\boldsymbol{T}}_s(\widehat{\boldsymbol{d}}) = \boldsymbol{0} \qquad \text{in } \widehat{\Omega}_s, \tag{1e}$$

$$\widehat{\boldsymbol{d}}_f = \widehat{\boldsymbol{d}} \qquad \text{on } \widehat{\Sigma}, \tag{1f}$$

$$-\Delta \widehat{\boldsymbol{d}}_f = \boldsymbol{0} \qquad \text{in } \Omega_f^t, \tag{1g}$$

where ρ_f and ρ_s are the fluid and solid densities, together with suitable initial and boundary conditions. In particular, in what follows we report the Robin

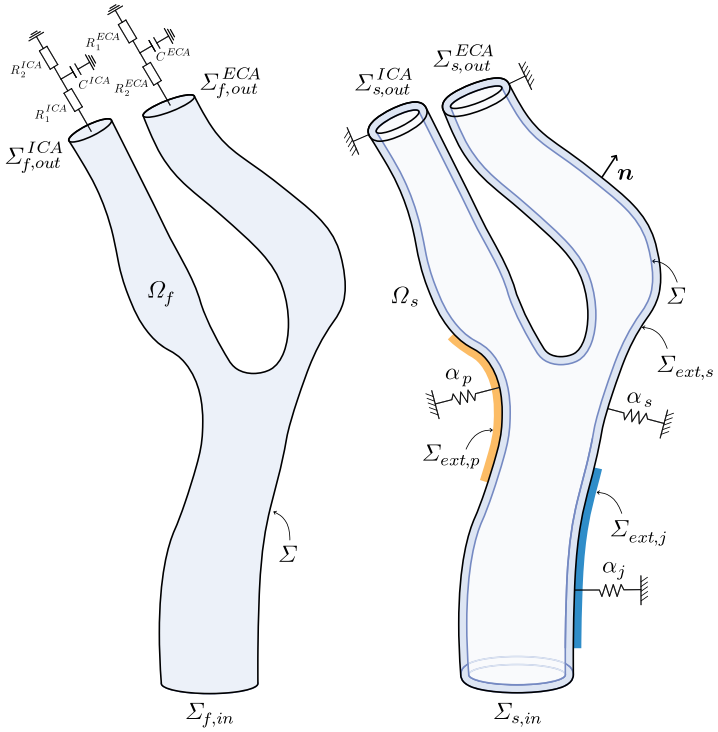

Figure 2: Fluid and structure domains. Highlighted, the area of the external wall surrogating the plaque (in yellow) and the area of contact with the jugular vein (in blue).

boundary conditions on $\widehat{\Sigma}_{ext,s} \cup \widehat{\Sigma}_{ext,j} \cup \widehat{\Sigma}_{ext,p}$ proposed here to model the support of external tissues and the plaque:

$$\alpha_s \widehat{\boldsymbol{d}} + \widehat{\boldsymbol{T}}_s(\widehat{\boldsymbol{d}})\widehat{\boldsymbol{n}} = P_{ext}\widehat{\boldsymbol{n}} \qquad \text{on } \widehat{\Sigma}_{ext,s}, \tag{2a}$$

$$\alpha_j \widehat{\boldsymbol{d}} + \widehat{\boldsymbol{T}}_s(\widehat{\boldsymbol{d}})\widehat{\boldsymbol{n}} = P_{ext}\widehat{\boldsymbol{n}} \qquad \text{on } \widehat{\Sigma}_{ext,j}, \tag{2b}$$

$$\alpha_p \widehat{\boldsymbol{d}} + \widehat{\boldsymbol{T}}_s(\widehat{\boldsymbol{d}})\widehat{\boldsymbol{n}} = P_{ext}\widehat{\boldsymbol{n}} \qquad \text{on } \widehat{\Sigma}_{ext,p}. \tag{2c}$$

Condition (2c) surrogates the presence of the atherosclerotic plaque by differentiating the parameter $\alpha_p = \alpha_p(\boldsymbol{x})$ with respect to the values $\alpha_s = \alpha_s(\boldsymbol{x})$ and $\alpha_j = \alpha_j(\boldsymbol{x})$ used to describe the elastic response of the surrounding tissues in correspondence of the healthy vessel and the jugular vein, respectively. In Eq. (2), P_{ext} represents the pressure in the neck.

Following a classical choice in haemodynamic applications, the ALE map was defined considering an harmonic extension operator (Eq. (1g)), so the displacement field at the boundary $\boldsymbol{d}|_{\Sigma^t}$ is extended into Ω_f^t to obtain the fluid domain displacement $\boldsymbol{d}_f$ and velocity $\boldsymbol{u}_f = \dot{\boldsymbol{d}}_f$. This introduces a geometric coupling given by condition (1f). Conditions (1c)-(1d) are the kinematic and dynamic fluid-structure interface conditions, respectively.

In Eq. (1a), the fluid Cauchy stress tensor is defined by

$$\boldsymbol{T}_f(\boldsymbol{u}, p) = -p\boldsymbol{I} + \mu_f \left(\nabla \boldsymbol{u} + (\nabla \boldsymbol{u})^T \right),$$

where μ_f is the fluid viscosity.

In Eq. (1e), $\widehat{\boldsymbol{T}}_s$ is the solid Piola-Kirchhoff stress tensor. We considered a neo-Hookean model to describe the solid, where the Cauchy stress tensor is given by

$$\boldsymbol{T}_s(\boldsymbol{d}) = \frac{\lambda}{2}\left(J - \frac{1}{J}\right)\boldsymbol{I} + \frac{\mu_s}{J}\left(\widehat{\boldsymbol{F}}_s \widehat{\boldsymbol{F}}_s^T - \boldsymbol{I}\right),$$

where μ_s is the shear modulus, λ is Lamé's first parameter, $\widehat{\boldsymbol{F}}_s$ is the deformation gradient tensor, and $J = det(\widehat{\boldsymbol{F}}_s)$. This model is known not to be accurate for the computation of Von Mises stresses. However, we believe that it is a suitable choice for our aims, since we were interested mainly in fluid-dynamic quantities. Moreover, the displacements are not so large to require an anisotropic model. Accordingly, the choice of a neo-Hookean constitutive law has been considered in many FSI studies of fluid-dynamics in carotids in presence of plaque (Li et al. 2006; Kock et al. 2008; Tao et al. 2015).

2.2 Other boundary conditions and numerical details

2.2.1 Structure/fluid mesh boundary conditions

The boundary of the solid domain $\partial\widehat{\Omega}_s$ is completed by the inlet and outlet rings $\widehat{\Sigma}_{s,in}$, $\widehat{\Sigma}_{s,out}^{ICA}$ and $\widehat{\Sigma}_{s,out}^{ECA}$.

The corresponding boundary conditions prescribed on $\widehat{\Sigma}_{s,in}$ a tangential homogeneous Neumann boundary condition to allow movement of the inlet in the tangential directions $\boldsymbol{\tau}_j$, $j = 1, 2$, and a homogeneous Dirichlet boundary condition in the normal direction:

$$(\widehat{\boldsymbol{T}}_s \widehat{\boldsymbol{n}}) \cdot \widehat{\boldsymbol{\tau}}_j = \boldsymbol{0}, \quad j = 1, 2 \qquad \text{on } \widehat{\Sigma}_{s,in}, \tag{3a}$$

$$\widehat{\boldsymbol{d}} \cdot \widehat{\boldsymbol{n}} = \boldsymbol{0} \qquad \text{on } \widehat{\Sigma}_{s,in}. \tag{3b}$$

A homogeneous Dirichlet boundary condition for all the components was instead prescribed on $\widehat{\Sigma}_{s,out}^{ICA}$ and $\widehat{\Sigma}_{s,out}^{ECA}$:

$$\widehat{\boldsymbol{d}} = \boldsymbol{0} \qquad \text{on } \widehat{\Sigma}_{s,out}^{ICA} \cup \widehat{\Sigma}_{s,out}^{ECA}. \tag{4}$$

Accordingly, for the fluid domain problem we prescribed on $\widehat{\Sigma}_{f,in}$ a tangential homogeneous Neumann condition and a normal homogeneous Dirichlet condition:

$$\nabla \widehat{\boldsymbol{d}}_f \widehat{\boldsymbol{n}} \cdot \widehat{\boldsymbol{\tau}}_j = \boldsymbol{0}, \quad j = 1, 2 \qquad \text{on } \widehat{\Sigma}_{f,in}, \tag{5a}$$

$$\widehat{\boldsymbol{d}}_f \cdot \widehat{\boldsymbol{n}} = \boldsymbol{0} \qquad \text{on } \widehat{\Sigma}_{f,in}. \tag{5b}$$

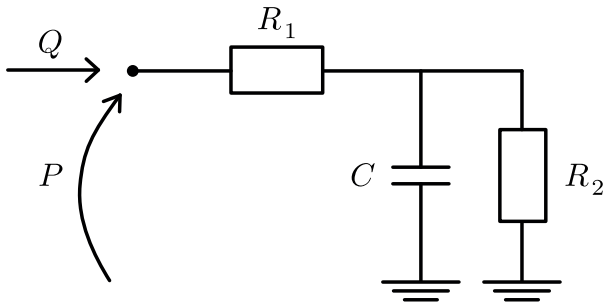

Figure 3: 3-element windkessel model used to represent the behaviour of the downstream vasculature.

2.2.2 Fluid boundary conditions

The boundary of the fluid domain $\partial\Omega_f^t$ is made up of the inlet section $\Sigma_{f,in}^t$, two outlet sections $\Sigma_{f,out}^{ICA}$ and $\Sigma_{f,out}^{ECA}$ of the internal (ICA) and external carotid arteries (ECA), respectively, and the interface Σ^t. We detail here the boundary conditions prescribed at the fluid inlet and outlets.

Inlet boundary condition On the inlet section $\Sigma_{f,in}^t$ we considered patient-specific conditions based on flow rates:

$$\int_{\Sigma_{f,in}^t} \boldsymbol{u} \cdot \boldsymbol{n}\, d\sigma = Q_{in}.$$

The values of $Q_{in}(t)$ were obtained from ECD measurements, as discussed in (Guerciotti et al. 2015; Domanin et al. 2017b). To prescribe the previous condition, each flow rate was mapped to a pseudo-parabolic velocity profile, leading to a Dirichlet boundary condition:

$$\boldsymbol{u} = \boldsymbol{g}_{in} \qquad \text{on } \Sigma_{f,in}^t. \tag{6}$$

where $\boldsymbol{g}_{in}$ was chosen such that $\int_{\Sigma_{f,in}^t} \boldsymbol{g}_{in} \cdot \boldsymbol{n}\, d\sigma = Q_{in}$.

Outlet boundary conditions Outlet boundary conditions on $\Sigma_{f,out}^{ICA}$ and $\Sigma_{f,out}^{ECA}$ were modeled using a *geometric multiscale* approach, where a zero-dimensional model was coupled to each of the outlets of the three-dimensional domain in order to describe the downstream vasculature. In particular, we considered here a 3-element windkessel lumped parameter model, which provides a dynamic relationship between outlet pressure and flow for the FSI solution (Westerhof et al. 2008) (see Fig. 3).

The corresponding differential equation linking pressure and flow for the generic outflow $\Sigma_{f,out}$ is the following:

$$\frac{d\,(P - R_1 Q)}{dt} + \frac{1}{R_2 C}\,(P - R_1 Q) = \frac{Q}{C}\ ,$$

where R_1 represents the proximal resistance, R_2 the distal resistance and C the distal compliance. Applying the method of integrating factors, its analytical solution can be written as (Quarteroni et al. 2016)

$$P(t) = R_1 Q(t) + (P(0) - R_1 Q(0))\, e^{-\frac{t}{R_2 C}} + \frac{1}{C}\int_0^t Q(\tau) e^{-\frac{\tau - t}{R_2 C}}\, d\tau. \qquad (7)$$

Setting $P = -\frac{1}{|\Sigma_{f,out}|}\int_{\Sigma_{f,out}} \boldsymbol{T}_f(\boldsymbol{u}, p)\boldsymbol{n}\cdot\boldsymbol{n}\, d\sigma$ and $Q = \rho_f \int_{\Sigma_{f,out}} \boldsymbol{u}\cdot\boldsymbol{n}\, d\sigma$ (Quarteroni et al. 2016), Eq. (7) can be interpreted as a resistance condition for the FSI problem.

In a time-discrete setting, Eq. (7) is applied over the timeline of a single time step, from t^n to t^{n+1}. At time t^{n+1}, the flow rate Q is unknown, thus a possible solution is given by evaluating the flow rate term through a suitable extrapolation from previous time steps. Setting $P(0) = 0$ and $Q(0) = 0$ (that is, starting from an unloaded system), using a first-order extrapolation for Q, and assuming the traction constant over $\Sigma_{f,out}$, we obtained the following Neumann boundary condition:

$$\boldsymbol{T}_f(\boldsymbol{u}^{n+1}, p^{n+1})\boldsymbol{n}\cdot\boldsymbol{n} = R_1\rho_f \int_{\Sigma_{f,out}} \boldsymbol{u}^n\cdot\boldsymbol{n}\, d\sigma + \frac{1}{C} I(t^n) \qquad \text{on } \Sigma_{f,out}, \qquad (8)$$

where $I(t^n)$ is the numerical approximation of the integral between t^n and t^{n+1} appearing in Eq. (7), which can be approximately computed through a quadrature rule (e.g. trapezoidal rule). To complete (8), we prescribed a null traction along the tangential directions.

The parameters of the windkessel model for each outlet $\Sigma_{f,out}^{ICA}$ and $\Sigma_{f,out}^{ECA}$ can be tuned to match available data, such as flow distribution between the branches and systolic and diastolic pressure data (Westerhof et al. 2008). In our application, in order to avoid the phenomenon of spurious reflections given by the truncation of the computational domain, we chose the value of R_1 as the one obtained in the case of a resistance absorbing boundary condition (Nobile and Vergara 2008):

$$R_1 = \sqrt{\frac{\rho_f \beta}{2}\frac{1}{A^{3/4}}},$$

where $\beta = \frac{h_s E}{(1-\nu^2)}\frac{\pi}{A}$, h_s is the structure thickness, A is the lumen radius at the given outlet, and E and ν are the Young modulus and the Poisson coefficient. We recall that the absorbing condition was derived by assuming a linear thin solid, but it was proven to be effective when coupled with any solid model choice (Nobile and Vergara 2008; Nobile et al. 2013).

This choice allowed us to tune only the two parameters R_2 and C for each outlet, along with parameters α_s, α_j and α_p in the external Robin boundary condition, to match reference lumen-wall boundary displacements obtained from imaging data, as explained in Section 3.

2.2.3 Numerical details

For the numerical solution of the FSI problem (1)-(2)-(3)-(5)-(4)-(6)-(8), we considered a first order time discretization for fluid, structure and kinematic conditions, with a semi-implicit treatment of the fluid convective term. The geometric coupling was treated explicitly, a strategy which is known to be stable and accurate in hemodynamics (Swim and Seshaiyer 2006; Fernández et al. 2007; Nobile et al. 2013; Quarteroni et al. 2017). The resulting FSI problem was solved monolithically by means of first order Finite Elements, stabilized by means of the SUPG-PSPG technique (Tezduyar 1991; Forti and Dedè 2015), with an inexact Newton method given by a block approximation of the Jacobian, leading to the split solution of fluid velocity, pressure and vessel wall unknowns (Crosetto et al. 2011; Deparis et al. 2016). This method has been shown to be highly scalable in the hemodynamic regime.

3 Methods for processing imaging data

Three subjects (P1, P2, P3 in what follows) were selected for this study. All carotids were evaluated by means of ECD and MRI acquisitions. All patients featured a stenosis at the level of the ICA (70% for P1, 80% for P2 and P3) and were followed at Fondazione IRCSS Ca' Granda, Ospedale Maggiore Policlinico, Milan, in particular at the Vascular Surgery Operative Unit for the ECD acquisitions and at the Operative Unit of Radiology for the MRI acquisitions.

3.1 Characteristics of image data

Carotid bifurcations were sampled with ECD using an iU22 ultrasound scanner and linear 8MHz probe (Philips Ultrasound, Bothell, WA). For more details regarding the ECD acquisitions, we refer to Guerciotti et al. 2015 and Domanin et al. 2017b.

MRI acquisitions were performed with a Siemens 1.5T Avanto scanner (Siemens Healthcare, Hoffman Estates, IL) with the following sequences and parameters:

- 3D Fat-suppressed T1-weighted Gradient-Echo images in the coronal plane, from now on referred to as 3D-FLASH MRI (repetition time (TR) = 3.13, echo-time (TE) = 1.14, flip-angle = 25°, matrix = 384 × 346 × 230), acquired before and during injection of paramagnetic contrast medium (gadolinium). The in-plane resolution is $0.84 \times 0.84\,mm$ and the slice thickness is $1\,mm$;

- 2D TurboFLASH retrospectively electrocardiography-gated images in the axial plane, from now on referred to as CINE MRI (TR = 46.35, ET = 1.3, flip-angle = 70°, matrix = 272 × 245). The in-plane resolution is $1.1 \times 1.1\,mm$ and the slice thickness is $6\,mm$. For each acquisition plane, 18 (for P3) or 25 (for P1 and P2) phases were reconstructed throughout the

cardiac cycle, obtaining a temporal resolution of 28 - 48 ms. The discrete time instants of acquisition is generically denoted by t_k;

- Turbo spin-echo (TSE) T1-weighted axial images (TR = 7.50, TE = 8.9, flip-angle = 144°, slice thickness = $4\,mm$, matrix = 320×224).

3.2 Geometry reconstruction

Three-dimensional carotid geometries were reconstructed from 3D-FLASH MRI images. Segmentation was performed using a level-set technique (`www.vmtk.org`; Antiga et al. (2008); Izzo et al. (2018)) with a colliding fronts initialization. The surface mesh of the lumen boundary was extracted as the zero-level isosurface through the marching cubes algorithm (Lorensen and Cline 1987). For each patient, the surface model was successively discretized into a fluid mesh of tetrahedra. Since the resolution of available MRI data was not suitable to detect the vessel wall, the structure domain was generated by extruding the surface mesh of the lumen boundary in order to obtain a realistic thickness for the vessel wall (10% of the diameter, Harloff et al. (2009)). The computational meshes are made up of 160k, 187k, 220k fluid tetrahedra and 128k, 124k, 170k solid tetrahedra, for P1, P2, P3, respectively. This corresponds to a representative value of the space discretization h, which is $0.1\,cm$ far from the stenosis and $0.04\,cm$ at the stenosis (about 8% of the respective diameters).

Based on the localization of the stenosis, on the analysis of TSE images (see Fig. 4, a) and on consultations with physicians, we were able to localize the region $\Sigma_{ext,p}$ in the external structure boundary corresponding to the plaque. In view of the estimation of parameter α, detailed in Section 3.5, we divided the remaining external boundary of the structure mesh into two (possibly non-connected) regions $\Sigma_{ext,s}$ and $\Sigma_{ext,j}$, identifying the surrounding tissues and the area of contact with the jugular vein, respectively (see Fig. 4, c and d).

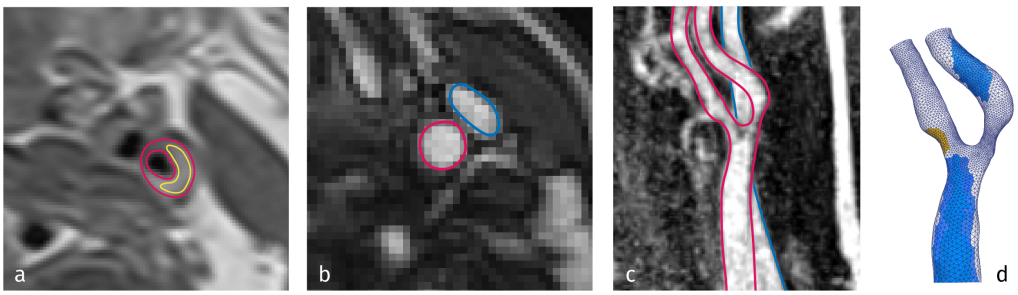

Figure 4: From left to right: a) TSE image; b) CINE MRI; c) 3D-FLASH MRI. In all images the carotid lumen and external wall are shown in fuchsia, the plaque bulk in yellow and the jugular vein in blue; d) Computational structure mesh. $\Sigma_{ext,s}$ in white, $\Sigma_{ext,j}$ in blue, $\Sigma_{ext,p}$ in yellow.

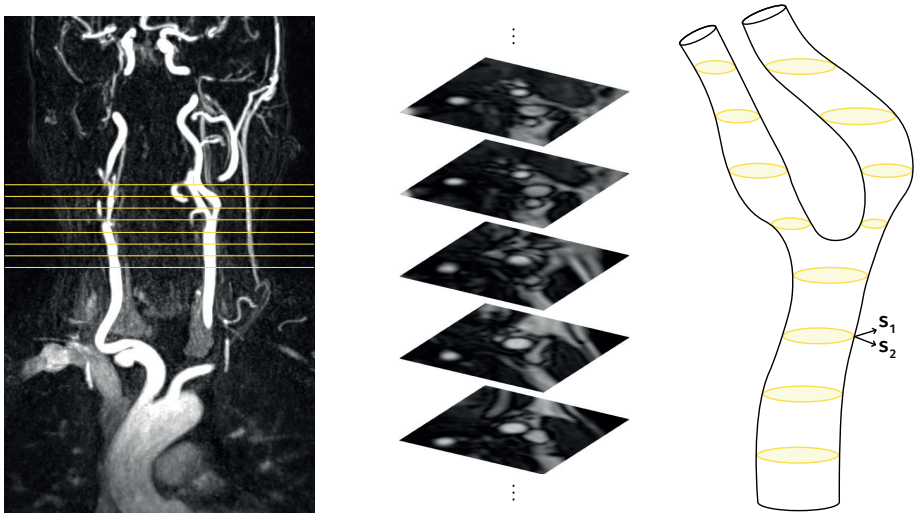

Figure 5: CINE MRI acquisition planes viewed on a 3D-FLASH image (left and middle) and corresponding position on the carotid (right).

3.3 CINE MRI processing

As observed in Section 2, the optimization procedure to find suitable values for the elastic parameters α_s, α_j and α_p was based on planar displacements of the lumen-wall boundary, which were obtained from CINE MRI images (see Fig. 4, b).

Axial acquisition planes were positioned $6\,mm$ apart covering a region centered in the bifurcation with a dimension of $5-6\,cm$, giving a total of $8-10$ slices for each patient (see Fig. 5). Before image processing, the datasets were evaluated to assess image quality. A limited number of acquisitions which were affected by noise, slices in which the carotid cross-section was too slanted or where the carotid exhibited an excessive in-plane rigid translation were neglected. For all remaining slices, a segmentation procedure was applied to all time frames in order to obtain the displacements required for the parameter estimation. Image segmentation and contour processing were performed with an in-house code developed using the Matlab Image Processing Toolbox (Natick, MA).

As a first processing step, a region of interest (ROI) was delineated around the cross-section of the carotid (see Fig. 6, a). Since the segmentation procedure is pixel-based, the position of the contour points and, as a consequence, the computed values of displacement are strictly related to the spatial resolution of the available CINE MRI data. In order to avoid the potential clipping of the displacements, the images were upsampled using bilinear interpolation to increase their resolution from the original $1.1 \times 1.1\,mm$. Image contrast was enhanced (see Fig. 6, b) to ease the automatic segmentation. A thresholding operation was applied to the grayscale image, obtaining the corresponding binary image by clustering the original gray-level intensity values into two classes (in

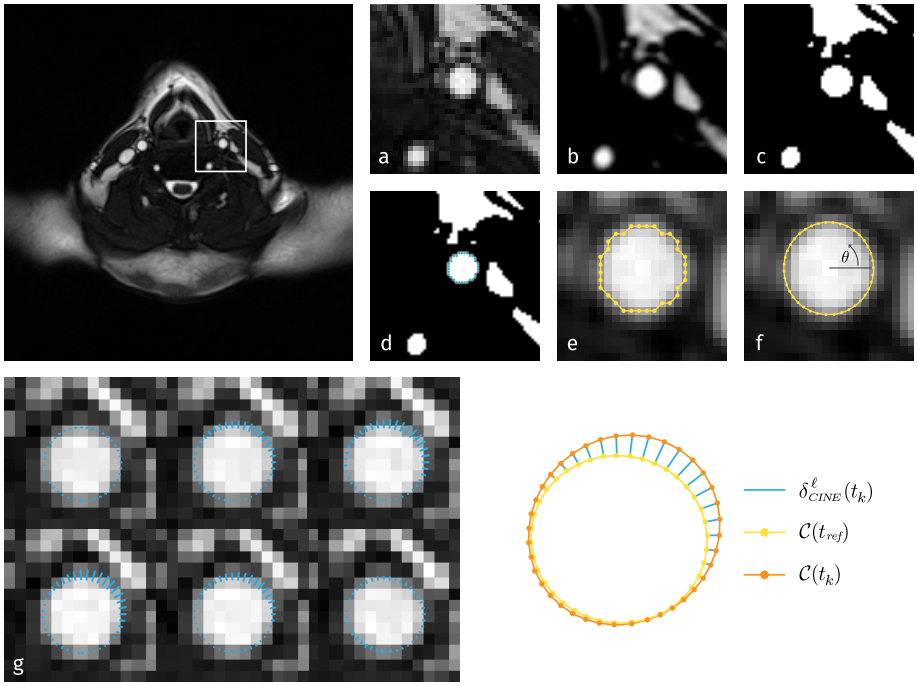

Figure 6: Automatic segmentation of CINE MRI images. a) Selection of the ROI; b) Upsampling and contrast enhancement; c) Thresholded binary image; d) Resulting segmented boundary; e) Jagged contour; f) Approximated smooth contour; g) Lumen-wall boundary displacements δ^{ℓ}_{CINE} (in light blue) for selected time instants t_k throughout the cardiac cycle.

black and in white in Fig. 6, c). This operation was done through the application of Otsu's method (Otsu 1979), an iterative procedure that looks for the optimal gray-level threshold able to separate the image pixels by minimizing the intra-class intensity variance. For each acquisition plane, the contour of the carotid was then made up of all points positioned in the pixel centers placed on the boundary between black and white (see Fig. 6, d).

Given the small dimension of the carotid diameter with respect to the image resolution, such segmented contours could feature a jagged boundary (see Fig. 6, e). In order to regularize the contours, we approximated them by fitting a closed curve $\mathcal{C}(t)$ for each time t in the cardiac cycle. Writing $\mathcal{C}(t)$ in polar coordinates, $(x(t), y(t))$ belongs to $\mathcal{C}(t)$ if

$$\begin{cases} x(t) = x_0 + r(\theta, t)\, cos(\theta) \\ y(t) = y_0 + r(\theta, t)\, sin(\theta) \end{cases} \qquad \theta \in [0, 2\pi],$$

where (x_0, y_0) is the average location of the contour centroid over the cardiac cycle. Representing $r(\theta, t)$ through a Fourier decomposition of order N, we have

for each k:

$$r(\theta, t) = \sum_{j=0}^{N} \left(a_j(t)\, cos(j\theta) + b_j(t)\, sin(j\theta) \right), \tag{9}$$

for a suitable value of N (see Fig. 6, f), chosen in order to approximate the contour while retaining its features.

In order to compute the lumen-wall boundary displacements, the contour corresponding to the time frame of minimum filling was chosen as a reference (t_{ref}). For all other time frames, the displacements were computed as the normal distances between the current and the reference contours (see Fig. 6, g). This procedure was repeated for all available slices, obtaining for each slice ℓ the displacement $\delta^{\ell}_{CINE}(t, \theta)$, which is a scalar function of time and angular position.

3.4 Lumen-wall boundary displacement processing

Given the variability of the processed data, the pipeline explained in Section 3.3 was repeated several times by varying some of the processing parameters. In such a way, starting from the same dataset, we were able to provide a descriptive analysis of the displacements computed given different sets of processing parameters. In particular, different values were chosen for the image upsampling factor γ ($\gamma = 2, 4, 6, 8$) and for the order N of the Fourier decomposition in Eq. (9) needed to regularize the contours ($N = 2, 3$). In addition to this, both the original jagged contours and their smooth approximations (see Fig. 7, on the top) were considered for the computation of displacements. This resulted in 12 instances $\delta^{\ell,j}_{CINE}(t, \theta)$, $j = 1, \ldots, 12$, of the function δ^{ℓ}_{CINE} for each slice ℓ. For each of them, we considered a mean value over the contour, computed by considering a specific range Θ^{ℓ} of angular positions as follows:

$$\Delta^{\ell,j}_{CINE}(t) = \frac{1}{L^{\ell}} \int_{\Theta^{\ell}} \delta^{\ell,j}_{CINE}(t, \theta)\, d\theta, \tag{10}$$

where L^{ℓ} is the length of the portion of the contour parametrized by the angular position $\theta \in \Theta^{\ell}$. In such a way, we obtained for each time frame 12 values of $\Delta^{\ell,j}_{CINE}$, $j = 1, \ldots, 12$ (see Fig. 7, on the bottom left), one for each set of processing parameters. Starting from these families of curves, they were joined to produce a displacement band $\hat{\Delta}^{\ell}_{CINE}(t)$ for each slice ℓ, defined as

$$\hat{\Delta}^{\ell}_{CINE}(t) = \left\{ (t, \Delta^{\ell}_{CINE}) : \Delta^{\ell}_{CINE}(t) \in \left[\Delta^{\ell,min}_{CINE}(t), \Delta^{\ell,max}_{CINE}(t) \right] \right\},$$

where, for each t, $\Delta^{\ell,min}_{CINE}(t) = \min_{j=1,\ldots,12} \Delta^{\ell,j}_{CINE}(t)$ and $\Delta^{\ell,max}_{CINE}(t) = \max_{j=1,\ldots,12} \Delta^{\ell,j}_{CINE}(t)$ (see Fig. 7, on the bottom right). In view of the parameter estimation (see Section 3.5), we also introduced for each time t the mean value $\Delta^{\ell,mean}_{CINE}(t)$ and computed significant statistical indices such as point-wise variance and interquartile ranges. For our application, a more thorough analysis of temporal correlation between time frames was neglected.

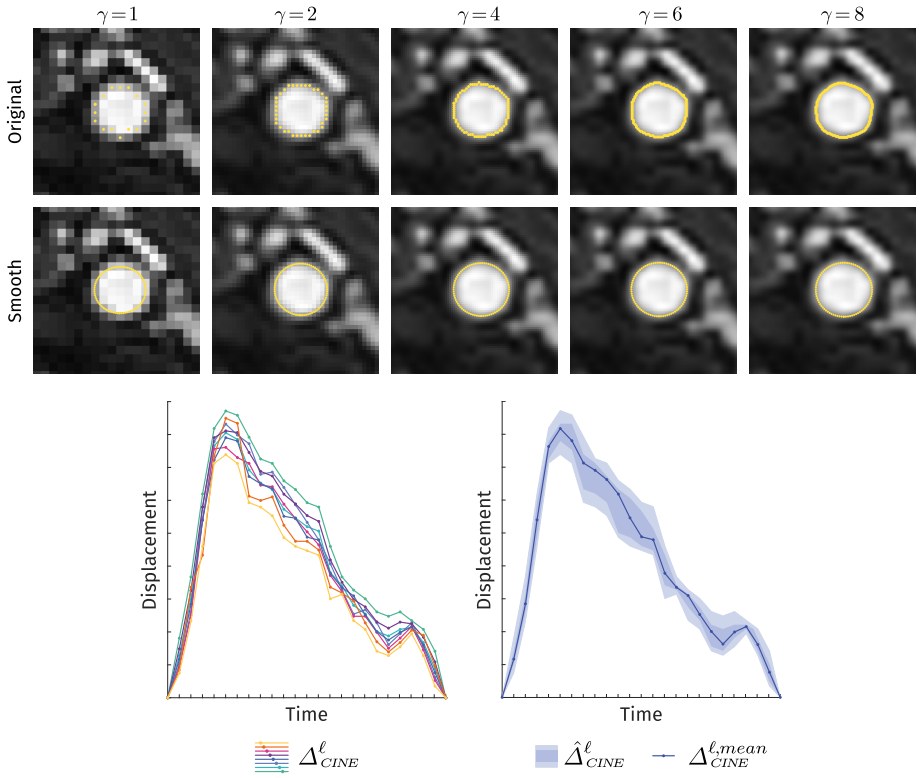

Figure 7: On the top, lumen-wall boundary contours shown for 5 values of the upsampling factor γ, both for the original jagged contours and for the smooth approximations. On the bottom, representative $\Delta^{\ell,j}_{CINE}$ curves (left) and corresponding displacement band $\hat{\Delta}^{\ell}_{CINE}$ (right). Also shown, its mean value $\Delta^{\ell,mean}_{CINE}$ and interquartile range, shown in darker blue.

3.5 Parameter estimation

The reference displacements $\Delta^{\ell,mean}_{CINE}(t)$ obtained from CINE MRI were used to tune a subset of model parameters. In particular, we estimated the values of α_s, α_j and α_p in the structure external Robin boundary condition (see Section 2.1) and of R_2 and C in the windkessel boundary condition (see Section 2.2.2). As regards the other parameters, such as the elastic properties of the healthy vessel and intermediate layer, we considered standard values taken from literature. While these parameters still exhibit inter-subject variability, we chose to focus on the estimation of parameters that are essential for the description of a pathological condition through our surrogate model.

In view of the parameter estimation, the vessel wall displacements $\boldsymbol{d}_h^n \simeq \boldsymbol{d}_h(t^n)$, resulting from the discretizations of FSI simulations, were sampled at each acquisition time t^k on the fluid-structure interface Σ^k on planes corresponding to the acquisition planes of CINE MRI images. Here, we denote with

Σ^k the approximation of the interface Σ^{t^k} after discretization. Since comparison between computed and measured displacements was possible only for in-plane displacements, the through-plane component of the FSI displacements was neglected. In such a way, for each slice ℓ and time t^k, the in-plane displacement scalar function $\delta_h^{\ell,k}(\theta)$ was obtained from FSI simulations as follows:

$$\delta_h^{\ell,k}(\theta) = \left(\sum_{i=1}^{2} \left(\boldsymbol{d}_h^k \Big|_{\Sigma^k} \cdot \boldsymbol{s}_i \right)^2 \right)^{\frac{1}{2}},$$

where $\boldsymbol{s}_i$, $i = 1, 2$, represent the versors lying on the CINE MRI acquisition planes (Fig. 5). Starting from this function, a mean value over Θ^ℓ was computed as follows:

$$\Delta_h^{\ell,k} = \frac{1}{L^\ell} \int_{\Theta^\ell} \delta_h^{\ell,k}(\theta)\, d\theta.$$

The values of α_s, α_j, α_p, R_2 and C were then estimated in order to minimize the discrepancies between $\Delta_h^{\ell,k} = \Delta_h^{\ell,k}(\boldsymbol{w}_h^k(q))$ and the reference displacements $\Delta_{CINE}^{\ell,mean}(t^k)$, where $\boldsymbol{w}_h^k = (\boldsymbol{u}_h^k, p_h^k, \boldsymbol{d}_h^k)$ is the FSI numerical solution and $q = (\alpha_s, \alpha_j, \alpha_p, R_2, C)$. Indicating with a $\widetilde{\ }$ the optimized parameters, the optimization problem for the parameter estimation then reads: find $\widetilde{q} = (\widetilde{\alpha}_s, \widetilde{\alpha}_j, \widetilde{\alpha}_p, \widetilde{R}_2, \widetilde{C})$ such that

$$\widetilde{q} = \arg\min_q \sum_{\ell,k} \left| \Delta_h^{\ell,k}(\boldsymbol{w}_h^k(q)) - \Delta_{CINE}^{\ell,mean}(t^k) \right|^2, \tag{11}$$

with $\boldsymbol{w}_h^k$ subjected to the time-discretization of system (1).

In order to solve the optimization problem (11) we considered a basic *direct search* method based on the *Hooke and Jeeves* algorithm (Hooke and Jeeves 1961; Quarteroni et al. 2000), where an FSI problem is solved using a value of q that is iteratively adjusted. In particular, starting from a uniform value of α ($\alpha_s = \alpha_j = \alpha_p$) and values of R_2 and C taken from literature, we set the increment $\delta q = -\eta \delta E$, where E is the quadratic error appearing in (11) and η is a suitable acceleration parameter. At each iteration we then updated q as $q + \delta q$ and evaluate the new error E. We refer to Perego et al. (2011) and Bertoglio et al. (2012) for efficient strategies to solve inverse problems in the FSI context based on *gradient descent* and Kalman filters methods, respectively, applied however to synthetic data.

In order to check the significance of the optimal values estimated with this procedure, we verified for each case that $\Delta_h^{\ell,k}(\boldsymbol{w}^k(\widetilde{q}))$ is placed within the reference band $\hat{\Delta}_{CINE}^{\ell}(t^k)$.

4 Results and Discussion

In this section we present the results of the surrogate plaque model described in Section 2, obtained by the integration of CINE MRI images as described in Section 3.

All numerical simulations were performed with the Finite Element library *lifeV* (`www.lifev.org`). We considered a neo-Hookean material for the vessel wall, with parameters $\lambda = 9.31 \cdot 10^5 Pa$ and $\mu_s = 1.03 \cdot 10^5 Pa$. Moreover, we set $\rho_f = 1.06\, g/cm^3$, $\mu_f = 0.035\, g/cm \cdot s$ and $\rho_s = 1.20\, g/cm^3$. The time discretization parameter is $\Delta t = 10^{-3} s$.

From the descriptive statistical analysis of the displacement bands obtained from the segmentation of CINE MRI images, we had a representation of the variability of the processed data. The variability of the computed values of displacements justified our choice of reproducing the segmentation procedure for different sets of parameters. At the same time, for each of the time frames, which were processed separately, the displacements lay in a small range of values, with a relative standard deviation that remains below 0.65.

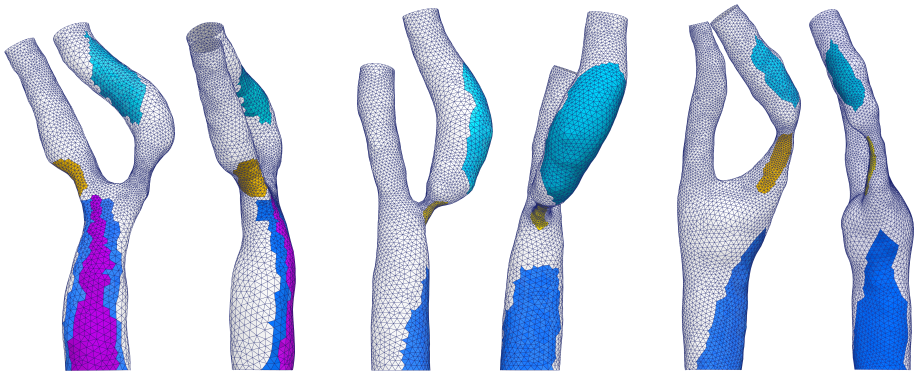

Figure 8: External boundary tags for P1 (left), P2 (center) and P3 (right). Plaque shown in yellow, jugular contact area in shades of blue, external tissues in white.

Table 1: Optimal external support parameter values set in patients P1, P2, P3 to account for the surrounding tissue (α_s), the jugular vein (α_j) and the plaque (α_p). Expressed in $g/(cm^2 \cdot s^2)$. The color code defined in Figure 8 is used to relate values to the corresponding wall regions.

	α_s	α_j	α_p
P1	$2.0 \cdot 10^6$ ☐	$0.5 \cdot 10^6$ ■ $1.8 \cdot 10^6$ ■ $1.5 \cdot 10^6$ ■	$4.0 \cdot 10^6$ ■
P2	$1.2 \cdot 10^6$ ☐	$8.0 \cdot 10^5$ ■ $2.0 \cdot 10^5$ ■	$3.2 \cdot 10^6$ ■
P3	$2.0 \cdot 10^6$ ☐	$1.2 \cdot 10^6$ ■ $1.0 \cdot 10^6$ ■	$4.0 \cdot 10^6$ ■

In Table 1 we report the results of the parameter estimation procedure regarding the surrogate plaque model and the external support of the jugular vein and other surrounding tissues. Approximately six iterations were required for each patient to obtain the optimized parameter values using our algorithm. Multiple regions were identified corresponding to the contact with the jugular vein, where different parameter values were used. A further parameter value was used for the overall support of other surrounding tissues (Fig. 8).

The parameter values used in the windkessel model coupled to both outlets (ECA and ICA) are reported in Table 2 for all patients.

Table 2: Windkessel model parameter values. Resistances expressed in $Pa/(cm^3 \cdot s)$, compliances expressed in $(Pa/cm^3)^{-1}$.

	ECA		ICA	
	R_2	C	R_2	C
P1	$2.0 \cdot 10^3$	$5.0 \cdot 10^{-3}$	$1.0 \cdot 10^3$	$4.0 \cdot 10^{-3}$
P2	$5.0 \cdot 10^3$	$1.0 \cdot 10^{-3}$	$1.0 \cdot 10^3$	$5.0 \cdot 10^{-3}$
P3	$2.0 \cdot 10^2$	$5.0 \cdot 10^{-3}$	$1.0 \cdot 10^3$	$1.0 \cdot 10^{-4}$

Fig. 9 shows the comparison between the computed displacements Δ_h^ℓ and the mean values of the lumen-wall boundary displacement $\Delta_{CINE}^{\ell,mean}$ computed from CINE MRI. In the same figure, we also report the lumen-wall boundary displacement bands $\hat{\Delta}_{CINE}^\ell$, highlighting their interquartile range. For all patients, we report the results obtained on slices located at the CCA and at its bifurcating branches (ECA and ICA). Notice that the sets Θ^ℓ of angular positions used in the computations of displacements (see (10)) correspond to the area of contact with the jugular vein for slices A, B, F in Fig. 9, whereas to the whole contour for the other slices. We focused our analysis on the systolic phase, when plaque is subjected to maximum stresses and then it is most at risk of rupture.

We notice that the computed displacements are in good agreement with the ones reconstructed from CINE MRI images. In particular, all the displacement curves lie in the uncertainty bands for almost all the time instants and for all the slices. This is in our opinion an excellent result, since the input of numerical simulations were given by another source of images with respect to CINE MRI (used here only for comparison), i.e. by ECD. To confirm this, in Table 3 we report the absolute and relative discrepancies between computed (Δ_h^ℓ) and measured ($\Delta_{CINE}^{\ell,mean}$) displacements, computed as root mean-squared errors. We point out that, in all patients, the error remains 1-2 orders of magnitude below the original image resolution ($1.1 \times 1.1\, mm$).

To further highlight the validity of our approach, we compared for patient P2 the results obtained with the parameter values obtained with our minimization

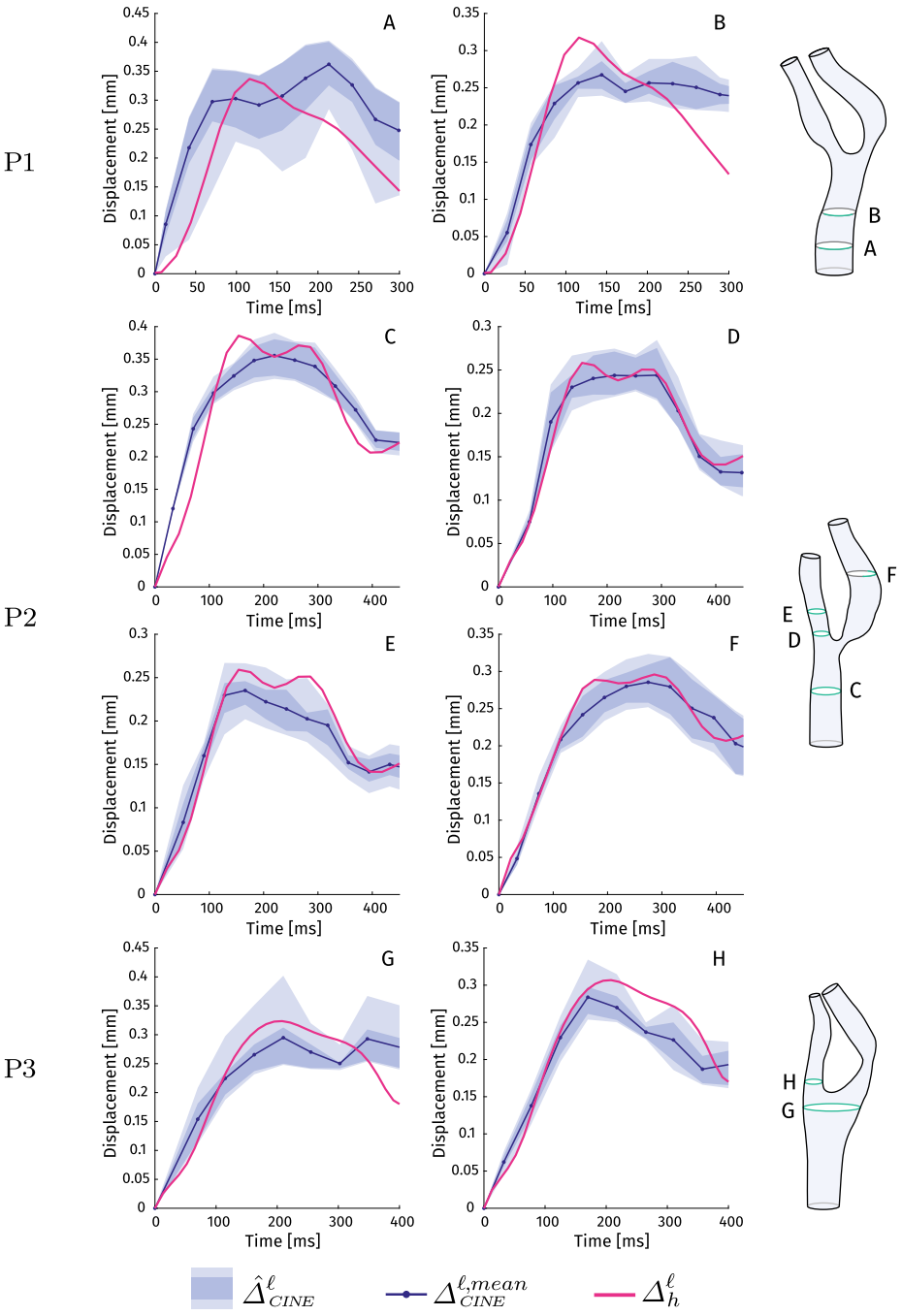

Figure 9: Comparison between computed displacements (shown in fuchsia) and reference lumen-wall boundary displacements obtained from CINE MRI (displacement bands $\hat{\Delta}^{\ell}_{CINE}$ and mean values $\Delta^{\ell,mean}_{CINE}$, shown in blue) for P1 (top), P2 (middle) and P3 (bottom). Displacements are computed on the contours highlighted in green.

Table 3: Evaluation of the discrepancies between computed and measured displacements, reported as absolute (mm) and relative (%) root mean-squared errors.

	Slice	Absolute error $[mm]$	Mean	Relative error [%]	Mean
P1	A	0.07	0.06	18.40	17.13
	B	0.04		15.85	
P2	C	0.04	0.03	11.47	11.25
	D	0.01		4.76	
	E	0.02		10.10	
	F	0.02		5.70	
P3	G	0.04	0.04	12.59	10.96
	H	0.03		9.34	

problem (configuration (i)) with two other scenarios regarding the choice of the elastic properties of the external support (surrounding tissues, jugular vein and plaque):

(ii) setting $\alpha_j = \alpha_s$, that is neglecting the presence of the jugular vein, and using values of α_s and α_p taken from configuration (i);

(iii) setting $\alpha_p = \alpha_j = \alpha_s$, that is neglecting both the jugular vein and the plaque, and using a value of α_s taken from configuration (i).

In Fig. 10 we report the corresponding results, which highlight that the inclusion of both the surrogate plaque model and the close-by jugular vein improved the agreement with the reference displacements. Indeed, considering a quantitative comparison, the average relative error obtained by including both the plaque and the jugular vein (11.25%) is almost half of those obtained in configurations (ii) and (iii) (21.15% and 19.96%, respectively). We observe in particular slice F, where neglecting the jugular vein lead to an error of about 40% in both scenarios.

To complete our analysis, in Fig. 11 we report some fluid dynamic quantities in order to highlight the disturbed flow arising as a consequence of the presence of the plaque. The evaluation of this disturbed flow, as obtained by our new surrogate model, is important to evaluate the risk of plaque rupture and the formation of transition to turbolence effects Lee et al. (2008); Lancellotti et al. (2017). To this aim, we report the velocity streamlines and WSS maps at the systolic peak for all patients. As expected, we observe a highly disturbed flow after the stenosis in the ICA, characterized by large vortices, and elevated WSS

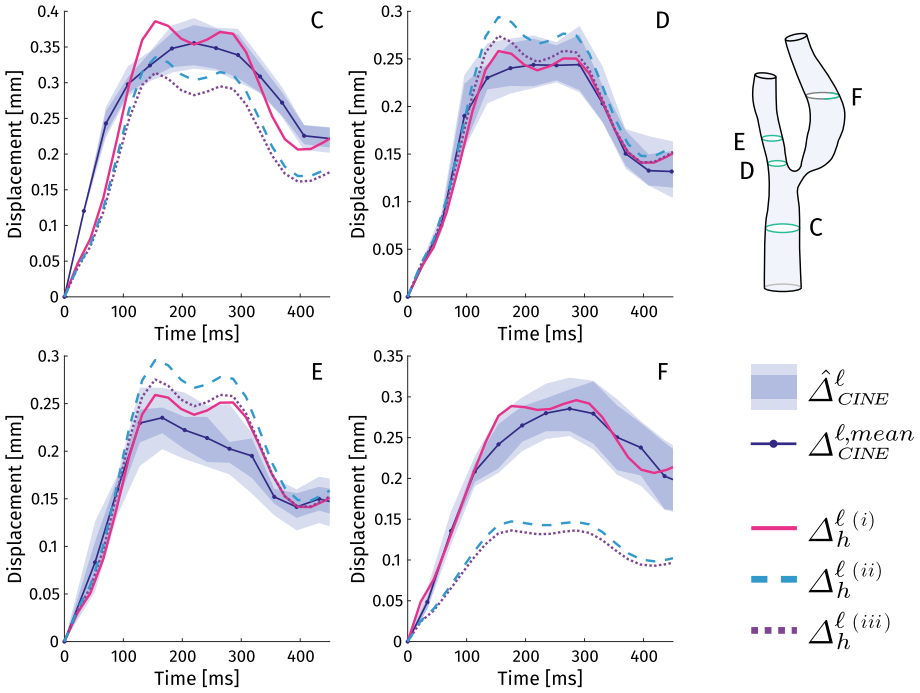

Figure 10: Comparison of lumen-wall boundary displacements for three simulation configurations: (i) External support differentiated into surrounding tissues, jugular vein and surrogate plaque model; (ii) $\alpha_j = \alpha_s$ (the jugular vein is neglected); (iii) $\alpha_p = \alpha_j = \alpha_s$ (both the jugular vein and the plaque are neglected).

values at the stenosis and at the ICA in the region where flow impinges on the artery wall.

5 Conclusions

In the present work we introduced a surrogate model for FSI in human carotid arteries based on the substitution of the atherosclerotic plaque modeling with a suitable boundary condition for the external structure surface, avoiding the complexities related to the geometric reconstruction and mechanical characterization of the plaque. To improve the accuracy, we also characterized the influence of the close-by jugular vein. To estimate the parameters in the surrogate model, we used CINE MRI data of structure displacement. We applied our approach to three subjects. In all cases, we found that describing the impact of both the plaque and the jugular vein improved the agreement of numerical results with CINE MRI data.

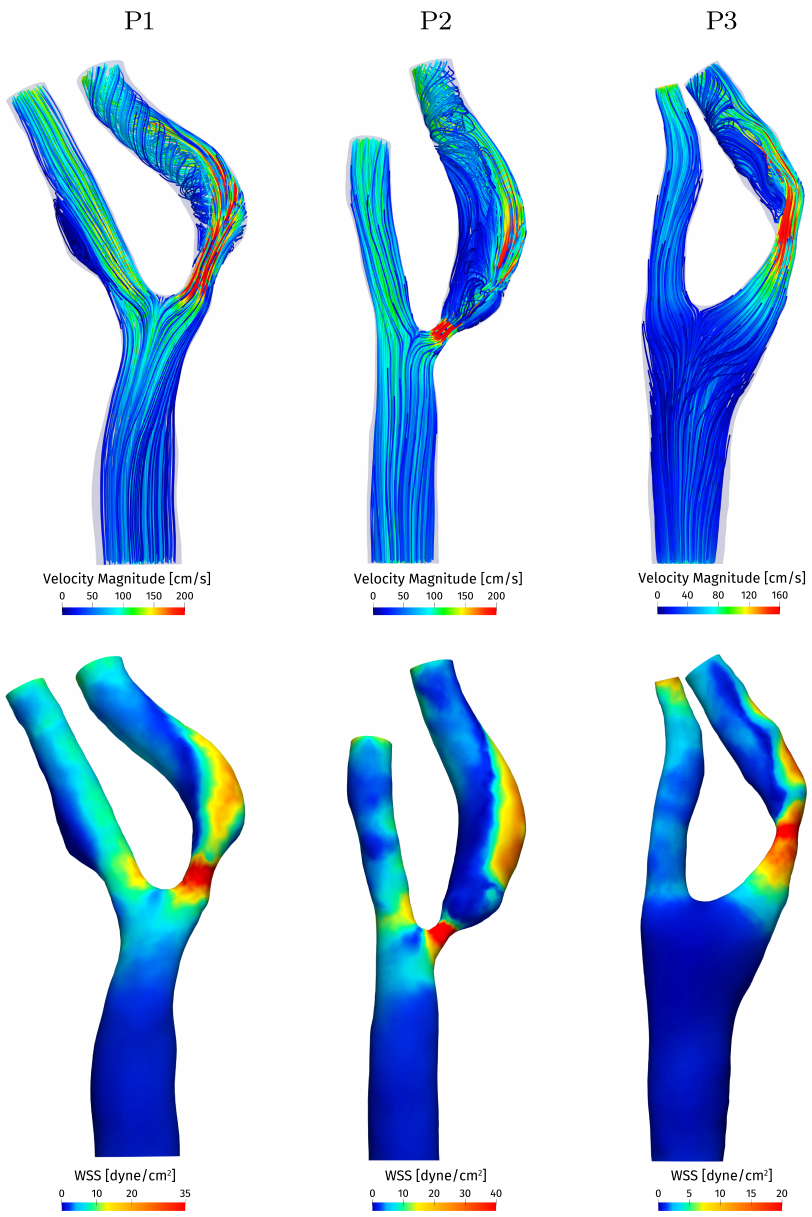

Figure 11: On the top, peak velocity streamlines. On the bottom, peak WSS maps.

References

Antiga L, Piccinelli M, Botti L, Ene-Iordache B, Remuzzi A, Steinman D (2008) An image-based modeling framework for patient-specific computational hemodynamics. Medical & Biological Engineering & Computing 46(11):1097–112, DOI 10.1007/s11517-008-0420-1

Baltes C, Hansen M, Tsao J, Kozerke S, Razavi R, Pedersen E, Boesiger P (2008) Determination of peak velocity in stenotic areas: Echocardiography versus k-t SENSE accelerated MR Fourier velocity encoding. Radiology 246(1):249–57, DOI 10.1148/radiol.2453061366

Bertoglio C, Moireau P, Gerbeau J (2012) Sequential parameter estimation for fluid—structure problems: Application to hemodynamics. International Journal for Numerical Methods in Engineering 28(4):434–455, DOI 10.1002/cnm.1476

Brinjikji W, Huston J, Rabinstein A, Kim GM, Lerman A, Lanzino G (2016) Contemporary carotid imaging: from degree of stenosis to plaque vulnerability. Journal of Neurosurgery 124(1):27–42, DOI 10.3171/2015.1.JNS142452.test

Crosetto P, Deparis S, Fourestey G, Quarteroni A (2011) Parallel algorithms for fluid-structure interaction problems in haemodynamics. SIAM Journal on Scientific Computing 33(4):1598–1622, DOI 10.1137/090772836

Deparis S, Forti D, Grandperrin G, Quarteroni A (2016) Facsi: A block parallel preconditioner for fluid–structure interaction in hemodynamics. Journal of Computational Physics 327:700–718, DOI 10.1016/j.jcp.2016.10.005

Domanin M, Bissacco D, Le Van D, Vergara C (2017a) Computational fluid-dynamic analysis after carotid endarterectomy: Patch graft versus direct suture closure. Journal of Vascular Surgery 67(3):897–898, DOI 10.1016/j.avsg.2017.04.016

Domanin M, Buora A, Scardulla F, Guerciotti B, Forzenigo L, Biondetti P, Vergara C (2017b) Computational fluid-dynamic analysis after carotid endarterectomy: Patch graft versus direct suture closure. Annals of Vascular Surgery 44:325–335, DOI 10.1016/j.avsg.2017.04.016

Donéa J, Giuliani S, Halleux JP (1982) An arbitrary lagrangian-eulerian finite element method for transient dynamic fluid-structure interactions. Computer Methods in Applied Mechanics and Engineering 33:689–723, DOI 10.1016/0045-7825(82)90128-1

Fernández M, Gerbeau JF, Grandmont C (2007) A projection semi-implicit scheme for the coupling of an elastic structure with an incompressible fluid. International Journal for Numerical Methods in Engineering 69(4):794 – 821, DOI 10.1002/nme.1792

Forti D, Dedè L (2015) Semi–implicit BDF time discretization of the Navier–Stokes equations with VMS–LES modeling in a high performance computing framework. Computers & Fluids 117:168–182, DOI 10.1016/j.compfluid.2015.05.011

Gao H, Long Q, Graves M, Gillard J, Li ZY (2009) Carotid arterial plaque stress analysis using fluid-structure interactive simulation based on in-vivo magnetic resonance images of four patients. Journal of Biomechanics 42(10):1416–23, DOI 10.1016/j.jbiomech.2009.04.010

Groen H, Gijsen F, Lugt A, Ferguson M, Hatsukami T, van der Steen A, Yuan C, Wentzel J (2007) Plaque rupture in the carotid artery is localized at the high shear stress region: A case report. Stroke 38(8):2379–81, DOI 10.1161/STROKEAHA.107.484766

Groen H, Simons L, Bouwhuijsen Q, Bosboom E, Gijsen F, van der Giessen A, van de Vosse F, Hofman A, van der Steen A, Witteman J, Lugt A, Wentzel J (2010) MRI based quantification of outflow boundary conditions for computational fluid dynamics of stenosed human carotid arteries. Journal of Biomechanics 43(12):2332–8, DOI 10.1016/j.jbiomech.2010.04.039

Guerciotti B, Vergara C, Azzimonti L, Forzenigo L, Buora A, Biondetti P, Domanin M (2015) Computational study of the fluid-dynamics in carotids before and after endarterectomy. Journal of Biomechanics 49(1):26–38, DOI 10.1016/j.jbiomech.2015.11.009

Harloff A, Zech T, Frydrychowicz A, Schumacher M, Schöllhorn J, Hennig J, Weiller C, Markl M (2009) Carotid intima-media thickness and distensibility measured by MRI at 3T versus high-resolution ultrasound. European Radiology 19(6):1470–1479, DOI 10.1007/s00330-009-1295-8

Harrison G, How T, Poole R, Brennan J, Naik J, Vallabhaneni SR, Fisher R (2014) Closure technique after carotid endarterectomy influences local hemodynamics. Journal of Vascular Surgery 60(2):418–427, DOI 10.1016/j.jvs.2014.01.069

Heise M, Krüger U, Rückert R, Pfitzman R, Neuhaus P, Settmacher U (2003) Correlation of intimal hyperplasia development and shear stress distribution at the distal end-side-anastomosis, in vitro study using particle image velocimetry. European Journal of Vascular and Endovascular Surgery 26(4):357–66, DOI 10.1016/S1078-5884(02)00567-1

Hirt C, Amsden A, Cook J (1974) An arbitrary lagrangian–eulerian computing method for all flow speeds. Journal of Computational Physics 14(3):227–253, DOI 10.1016/0021-9991(74)90051-5

Hooke R, Jeeves T (1961) Direct search solution of numerical and statistical problem. Journal of the Association for Computing Machinery 8:212–229, DOI 10.1145/321062.321069

Hyun S, Kleinstreuer C, Archie J (2000) Computer simulation and geometric design of endarterectomized carotid artery bifurcations. Critical Reviews in Biomedical Engineering 28(1-2):53–59, DOI 10.1615/CritRevBiomedEng.v28.i12.100

Hyun S, Kleinstreuer C, Archie J (2003) Computational analysis of effects of external carotid artery flow and occlusion on adverse carotid bifurcation hemodynamics. Journal of Vascular Surgery 37(6):1248–1254, DOI 10.1016/S0741-5214(02)75326-3

Izzo R, Steinman D, Manini S, Antiga L (2018) The vascular modeling toolkit: A Python library for the analysis of tubular structures in medical images. Journal of Open Source Software 3(25):745, DOI 10.21105/joss.00745

Kamenskiy A, Pipinos I, Dzenis Y, Gupta P, Kazmi S, Mactaggart J (2013) A mathematical evaluation of hemodynamic parameters after carotid eversion and conventional patch angioplasty. American Journal of Physiology Heart and Circulatory Physiology 305(5):716–724, DOI 10.1152/ajpheart.00034.2013

Kock S, Nygaard JV, Eldrup N, Fründ ET, Klaerke A, Paaske W, Falk E, Kim W (2008) Mechanical stresses in carotid plaques using MRI-based fluid-structure interaction models. Journal of Biomechanics 41(8):1651–1658, DOI 10.1016/j.jbiomech.2008.03.019

Ku D, Giddens D, Zarins C, Glagov S (1985) Pulsatile flow and atherosclerosis in the human carotid bifurcation - positive correlation between plaque location and low and oscillating shear-stress. Arteriosclerosis 5(3):293–302, DOI 10.1161/01.ATV.5.3.293

Lancellotti R, Vergara C, Valdettaro L, Bose S, Quarteroni A (2017) Large eddy simulations for blood dynamics in realistic stenotic carotids. International Journal for Numerical Methods in Engineering 33(11):e2868, DOI 10.1002/cnm.2868

Leach J, Rayz V, Mofrad M, Saloner D (2009) An efficient two-stage approach for image-based FSI analysis of atherosclerotic arteries. Biomechanics and Modeling in Mechanobiology 9(2):213–223, DOI 10.1007/s10237-009-0172-3

Lee S, Lee SW, Fischer P, Bassiouny H, Loth F (2008) Direct numerical simulation of transitional flow in a stenosed carotid bifurcation. Journal of Biomechanics 41(11):2551–61, DOI 10.1016/j.jbiomech.2008.03.038

Lee S, Kang S, Hur N, Jeong SK (2012) A fluid-structure interaction analysis on hemodynamics in carotid artery based on patient-specific clinical data. Journal of Mechanical Science and Technology 26(12):3821–3831, DOI 10.1007/s12206-012-1008-0

Li ZY, Howarth S, Tang T, Gillard J (2006) How critical is fibrous cap thickness to carotid plaque stability?: A flow-plaque interaction model. Stroke 37:1195–1199, DOI 10.1161/01.STR.0000217331.61083.3b

Lorensen W, Cline H (1987) Marching cubes: A high resolution 3D surface construction algorithm. ACM SIGGRAPH Computer Graphics 21(4):163–169, DOI 10.1145/37401.37422

Makris G, Nicolaides A, Xu X, Geroulakos G (2010) Introduction to the biomechanics of carotid plaque pathogenesis and rupture: Review of the clinical evidence. The British Journal of Radiology 83(993):729–35, DOI 10.1259/bjr/49957752

Markl M, Wegent F, Zech T, Bauer S, Strecker C, Schumacher M, Weiller C, Hennig J, Harloff A (2010) In vivo wall shear stress distribution in the carotid artery effect of bifurcation geometry, internal carotid artery stenosis, and recanalization therapy. Circulation Cardiovascular imaging 3(6):647–55, DOI 10.1161/CIRCIMAGING.110.958504

Meyerson S, Skelly C, Curi M, Shakur U, Vosicky J, Glagov S, Schwartz L, Christen T, Gabbiani G (2001) The effects of extremely low shear stress on cellular proliferation and neointimal thickening in the failing bypass graft. Journal of Vascular Surgery 34(1):90–97, DOI 10.1067/mva.2001.114819

Mofidi R, Powell T, Crotty T, Sheehan S, Mehigan D, MacErlaine D, Keaveny T (2005) Increased internal carotid artery peak systolic velocity is associated with presence of significant atherosclerotic plaque instability independent of degree of ICA stenosis. International Journal of Angiology 14(2):74–80, DOI 10.1007/s00547-005-1079-1

Moireau P, Xiao N, Astorino M, Figueroa C, Chapelle D, Taylor C, Gerbeau JF (2011) External tissue support and fluid–structure simulation in blood flows. Biomechanics and Modeling in Mechanobiology 11(1-2):1–18, DOI 10.1007/s10237-011-0289-z

Morbiducci U, Gallo D, Massai D, Consolo F, Ponzini R, Antiga L, Bignardi C, Deriu M, Redaelli A (2010) Outflow conditions for image-based hemodynamic models of the carotid bifurcation: Implications for indicators of abnormal flow. Journal of Biomechanical Engineering 132(9):091,005, DOI 10.1115/1.4001886

Naylor R, Ricco JB, Borst G, Debus S, Haro J, Halliday A, Hamilton G, Kakisis J, Kakkos S, Lepidi S, Markus H, McCabe D, Roy J, Sillesen H, van den

Berg J, Vermassen F, ESVS Committee, Kolh P, Venermo M (2017) Management of atherosclerotic carotid and vertebral artery disease: 2017 clinical practice guidelines of the european society for vascular surgery (ESVS). European Journal of Vascular and Endovascular Surgery 55:3–81, DOI 10.1016/j.ejvs.2017.06.021

Nixon A, Gunel M, Sumpio B (2009) The critical role of hemodynamics in the development of cerebral vascular disease: A review. Journal of Neurosurgery 112:1240–1253, DOI 10.3171/2009.10.JNS09759

Nobile F, Vergara C (2008) An effective fluid-structure interaction formulation for vascular dynamics by generalized robin conditions. SIAM Journal on Scientific Computing 30:731–763, DOI 10.1137/060678439

Nobile F, Pozzoli M, Vergara C (2013) Time accurate partitioned algorithms for the solution of fluid-structure interaction problems in haemodynamics. Computers and Fluids 86:470–482, DOI 10.1016/j.compfluid.2013.07.031

Otsu N (1979) A threshold selection method from gray-level histograms. IEEE Transactions on Systems, Man and Cybernetics 9(1):62–66

Perego M, Veneziani A, Vergara C (2011) A variational approach for estimating the compliance of the cardiovascular tissue: An inverse fluid-structure interaction problem. SIAM Journal on Scientific Computing 33(3):1181–1211, DOI 10.1137/100808277

Perktold K, Resch M (1990) Numerical flow studies in human carotid artery bifurcations: Basic discussion of the geometric factor in atherogenesis. Journal of Biomedical Engineering 12:111–123, DOI 10.1016/0141-5425(90)90131-6

Ponzini R, Vergara C, Rizzo G, Veneziani A, Roghi A, Vanzulli A, Parodi O, Redaelli A (2010) Womersley number-based estimates of blood flow rate in doppler analysis: In vivo validation by means of phase-contrast MRI. IEEE Transactions on Biomedical Engineering 57:1807–15, DOI 10.1109/TBME.2010.2046484

Quarteroni A, Sacco R, Saleri F (2000) Numerical Mathematics. Springer

Quarteroni A, Veneziani A, Vergara C (2016) Geometric multiscale modeling of the cardiovascular system, between theory and practice. Computer Methods in Applied Mechanics and Engineering 302:193–252, DOI 10.1016/j.cma.2016.01.007

Quarteroni A, Manzoni A, Vergara C (2017) The cardiovascular system: Mathematical modelling, numerical algorithms and clinical applications. Acta Numerica 26:365–590, DOI 10.1017/S0962492917000046

Rossmann J, Berger S, Saloner D (2002) Numerical analysis of flow through a severely stenotic carotid artery bifurcation. Journal of Biomechanical Engineering 124:9–20, DOI 10.1115/1.1427042

Slager C, Wentzel J, Gijsen F, Thury A, Van der Wal A, Schaar J, Serruys P (2005) The role of shear stress in the destabilization of vulnerable plaques and related therapeutic implications. Nature Clinical Practice Cardiovascular Medicine 2:456–464, DOI 10.1038/ncpcardio0298

Sui B, Gao P, Lin Y, Jing L, Sun S, Qin H (2014) Hemodynamic parameters distribution of upstream, stenosis center, and downstream sides of plaques in carotid artery with different stenosis: a MRI and CFD study. Acta Radiologica 56(3):347–354, DOI 10.1177/0284185114526713

Swim E, Seshaiyer P (2006) A nonconforming finite element method for fluid-structure interaction problems. Computer Methods in Applied Mechanics and Engineering 195(17-18):2088–2099

Tang D, Yang C, Zheng J, Woodard P, Sicard G, Saffitz J, Yuan C (2004) 3D MRI-based multicomponent FSI models for atherosclerotic plaques. Annals of Biomedical Engineering 32:947–60, DOI 10.1023/B:ABME.0000032457.10191.e0

Tang D, Yang C, Canton G, Wu Z, Hatsukami T, Yuan C (2013) Correlations between carotid plaque progression and mechanical stresses change sign over time: A patient follow up study using MRI and 3D FSI models. Biomedical Engineering Online 12:105, DOI 10.1186/1475-925X-12-105

Tang D, Kamm R, Yang C, Zheng J, Canton G, Bach R, Huang X, Hatsukami T, Zhu J, Ma G, Maehara A, Mintz G, Yuan C (2014) Image-based modeling for better understanding and assessment of atherosclerotic plaque progression and vulnerability: Data, modeling, validation, uncertainty and predictions. Journal of Biomechanics 47(4):834–846, DOI 10.1016/j.jbiomech.2014.01.012

Tao X, Gao P, Jing L, Lin Y, Sui B (2015) Subject-specific fully-coupled and one-way fluid-structure interaction models for modeling of carotid atherosclerotic plaques in humans. Medical Science Monitor 21:3279–3290, DOI 10.12659/MSM.895137

Tezduyar TE (1991) Stabilized finite element formulations for incompressible flow computations. Advances in Applied Mechanics, vol 28, Elsevier, pp 1–44

Thomas J, Antiga L, Che S, Milner J, Steinman D, Spence JD, Rutt B, Steinman D (2005) Variation in the carotid bifurcation geometry of young versus older adults implications for geometric risk of atherosclerosis. Stroke 36:2450–2456, DOI 10.1161/01.STR.0000185679.62634.0a

Wang Q, Canton G, Guo J, Guo X, Hatsukami T, Billiar K, Yuan C, Wu Z, Tang D (2017) MRI-based patient-specific human carotid atherosclerotic vessel material property variations in patients, vessel location and long-term follow up. PLOS ONE 12:e0180,829, DOI 10.1371/journal.pone.0180829

Westerhof N, Lankhaar JW, Westerhof B (2008) The arterial windkessel. Medical and Biological Engineering and Computing 47:131–41, DOI 10.1007/s11517-008-0359-2

Xu K, Yu L, Wan J, Wang S, Lu H (2020) The influence of the elastic modulus of the plaque in carotid artery on the computed results of FFR CT. Computer Methods in Biomechanics and Biomedical Engineering pp 1–11, DOI 10.1080/10255842.2019.1710741

Yuan J, Teng Z, Feng J, Zhang Y, Brown A, Gillard J, Jing Z, Lu Q (2015) Influence of material property variability on the mechanical behaviour of carotid atherosclerotic plaques: A 3D fluid-structure interaction analysis: Material property variability and plaque mechanical behaviours. International Journal for Numerical Methods in Engineering 31(8):1–12, DOI 10.1002/cnm.2722

Zarins C, Giddens D, Bharadvaj B, Sottiurai V, Mabon R, Glagov S (1983) Carotid bifurcation atherosclerosis. quantitative correlation of plaque localization with flow velocity profiles and wall shear stress. Circulation Research 53:502–14, DOI 10.1161/01.RES.53.4.502

MOX Technical Reports, last issues

Dipartimento di Matematica
Politecnico di Milano, Via Bonardi 9 - 20133 Milano (Italy)

08/2020 Antonietti, P. F.; Facciolà, C.; Verani, M.
Polytopic Discontinuous Galerkin methods for the numerical modelling of flow in porous media with networks of intersecting fractures

12/2020 Azzolin, L.; Dede', L.; Gerbi, A.; Quarteroni, A.
Effect of fibre orientation and bulk value on the electromechanical modelling of the human ventricles

11/2020 Antonietti, P.F.; Facciola', C.; Houston, P.; Mazzieri, I.; Pennes, G.; Verani, M.
High-order discontinuous Galerkin methods on polyhedral grids for geophysical applications: seismic wave propagation and fractured reservoir simulations

10/2020 Bonaventura, L.; Carlini, E.; Calzola, E.; Ferretti, R.
Second order fully semi-Lagrangian discretizations of advection--diffusion--reaction systems

09/2020 Rea, F.; Ieva, F.,; Pastorino, U.; Apolone, G.; Barni, S.; Merlino, L.; Franchi, M.; Corrao, G.
Number of lung resections performed and long-term mortality rates of patients after lung cancer surgery: evidence from an Italian investigation

05/2020 Artioli, E.; Beiraoda Veiga, L.; Verani, M.
An adaptive curved virtual element method for the statistical homogenization of random fibre-reinforced composites

07/2020 Fumagalli, A.; Scotti, A.
Reactive flow in fractured porous media

06/2020 Domanin, M.; Piazzoli, G.; Trimarchi, S.; Vergara, C.
Image-based displacements analysis and computational blood dynamics after endovascular aneurysm repair

04/2020 Didkovskyi, O.; Azzone, G.; Menafoglio A.; Secchi P.
Social and material vulnerability in the face of seismic hazard: an analysis of the Italian case

03/2020 Ferro, N.; Micheletti, S.; Perotto, S.
Compliance-stress constrained mass minimization for topology optimization on anisotropic meshes